

Modeling Rotation in Electrical Machines

Lauri Kettunen, Stefan Kurz, Timo Tarhasaari, Ville Räisänen, Antti Stenvall, and Saku Suuriniemi

Department of Electrical Engineering and Electromagnetics, Tampere University of Technology, Tampere FI-33101, Finland

This paper is about finite element kind of modeling of movement in electromechanical devices, especially in rotating electrical machines. The presented approach relies on geometry and manifolds. With an appropriate choice of charts, the spatial and temporal discretizations become decoupled, which implies that the spatial finite element mesh no longer restricts the allowed time steps. However, the standard basis functions of finite elements are not always powerful enough to support large changes in the rotation angle, and therefore in case of thin air gaps, an intermediate approach between the lock-step method and the choice of charts is preferable. This is also demonstrated in the latter part of this paper by an induction machine test example.

Index Terms—Electromagnetic fields, finite elements, manifolds, metric tensor, motion, rotating electrical machines.

I. INTRODUCTION

SOLUTION of electromagnetic boundary value problems modeling rotating electrical machines is computationally an intensive task. This topic has been subjected to numerous studies for the last three decades, and there is still research ongoing. Early examples can be found in [1], where the air gap was treated analytically, and in [2], where a hybrid integral-finite element technique was proposed. Another approach involves Lagrange multipliers [3], which was recently improved by using biorthogonal shape functions [4]. The mortar element method is a related technique, where nonconforming finite element spaces are weakly coupled [5]. To give some more timely examples, in [6], a mesh decomposition algorithm is presented, to efficiently deal with motion by the lock-step method on parallel computers. In [7], a meshless Galerkin method is employed for the simulation of a three-phase induction motor, including motion. Since there is no notion of connectivity, such methods might deal better with changing geometry than classical finite-element methods. Another direction of research can be observed in [8] and [9], where overlapping finite elements are used to connect nonconforming meshes. Eventually, an overview of strategies to model rotating machines can be found in [10] and [11].

The standard approach, which underlies all the cited works, is to assume the classical framework with an Euclidean ambient space into which the electrical machine is embedded. Although such an approach is very much supported by our natural intuition, computers do not have an intuition. Therefore, intuitive techniques need not be the most efficient approach into computing.

In this paper, we take a modern mathematical perspective, which is centered around geometry and manifolds; compare [12]. We explain how the rotation of electrical machines can be modeled by holding the stator and rotor stationary with respect to the chosen coordinate system while the distances between the points may change. When solving numerically the underlying electromagnetic boundary value problem, the practical engineering advantage is the decoupling of the spatial and temporal discretizations of the boundary

value problem. Thus, for instance, the finite element mesh need not be reconstructed although the rotor moves. Furthermore, any time step becomes possible in lock-step techniques. In the same spirit, for instance, the vibration of a machine caused by magnetostriction can be modeled with a fixed coordinate finite element mesh.

The presented approach complements various existing techniques that have been proposed before to deal with motion in rotating electrical machines. For related ideas and more background on the exploitation of metric on manifolds see also [13].

II. SPACE, DISTANCES, AND MOTION

The key point behind the approach suggested in this paper is that the distances between the points in space need not be dictated by the employed coordinate system. Instead, the distances pertain to the (underlying point set of the) manifold where the actual electromagnetic model lives on. Coordinate systems only parametrize this point set. On the manifold the distances are specified by the so-called metric tensor.

Consider a 3-D model of a rotating electrical machine. While the machine rotates, the material points of the rotor and stator move with respect to each other and their mutual distances change with time. We model this point set as a $(3 + 1)$ -dimensional Euclidean space $E^3 \times E^1$. Formally we assume that the metric tensor g_E , the unit 3-form σ_E , and permeability μ_E are known in E^3 . Furthermore, we assume that material points can be identified, implying their mutual distances can be determined with the metric tensor g_E for each moment of time.

A Cartesian coordinate system labels all the points of E^3 with coordinates. The codomain of the coordinates are so-called 3-tuples such as $(x, y, z) \in \mathbb{R}^3$. The coordinate system also implies an instance of metric—however—not to E^3 but instead to \mathbb{R}^3 .

Although a coordinate system is typically chosen such that the metric tensor of E^3 becomes represented by an identity matrix in \mathbb{R}^3 , nothing compels the modeler to do so. Recognition of this is the key to model a rotating electrical machine with fixed coordinates. Rotation can be considered by a metric tensor in \mathbb{R}^3 that corresponds with the desired distances in E^3 while the coordinates are considered just as labels of the points. When solving numerically boundary value

Manuscript received August 9, 2012; revised October 4, 2013; accepted November 3, 2013. Date of publication January 23, 2013; date of current version April 4, 2014. Corresponding author: S. Kurz (e-mail: stefan.kurz@tut.fi).

Digital Object Identifier 10.1109/TMAG.2013.2290101

0018-9464 © 2013 IEEE. Personal use is permitted, but republication/redistribution requires IEEE permission.

See http://www.ieee.org/publications_standards/publications/rights/index.html for more information.

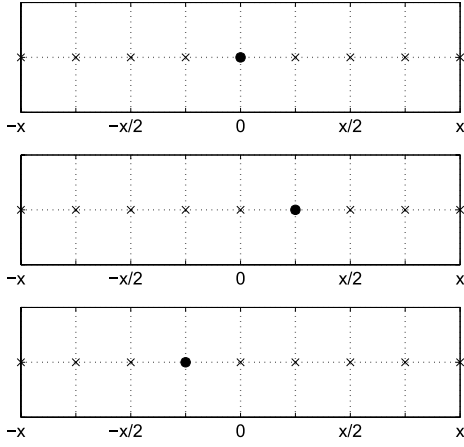


Fig. 1. Single material point (denoted by the dot) oscillates harmonically with respect to the boundary points in a bounded domain of 1-D Euclidean space. The crosses represent ruler ticks, and they can be employed to read the distance between the material point and the boundary points.

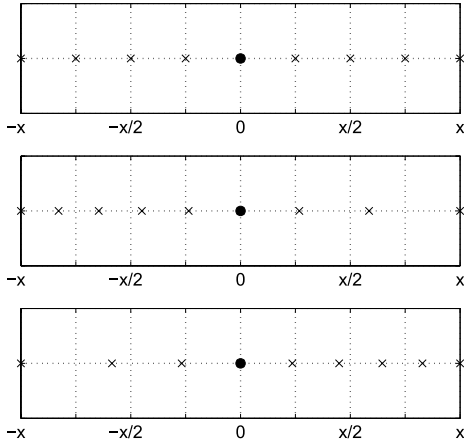


Fig. 2. Same oscillating material point as in Fig. 1, but this time, the coordinate of the material point is labeled as the origin and the desired spatial distances at each moment of time are specified by a metric tensor in \mathbb{R}^1 . Correspondingly, the coordinate of the material point is stationary, but the ruler ticks live with the motion.

problems this implies that the coordinates of the finite element mesh remain unchanged and therefore the mesh remains intact despite the rotation. This provides us with some advantages.

III. METRIC TENSOR AND DISTANCES

To demonstrate how the effect of motion is modeled into the metric tensor of \mathbb{R}^3 , let us pick a bounded domain of 1-D Euclidean space. We identify a single material point that oscillates harmonically in $E^1 \times E^1$, see Fig. 1. An immediate approach is to deal with the motion is to change the coordinate of the oscillating material point in time. However, an alternative is to label the material point as the origin and introduce a metric tensor that specifies the desired spatial distances at each moment of time, see Fig. 2.

In the 1-D case, the chosen metric tensor is represented in a given coordinate system by a 1×1 matrix \mathbf{G} . In case of Fig. 1, \mathbf{G} is an identity at every point, whereas in Fig. 2 it is not. In the same manner, in the $(2 + 1)$ -dimensional case the

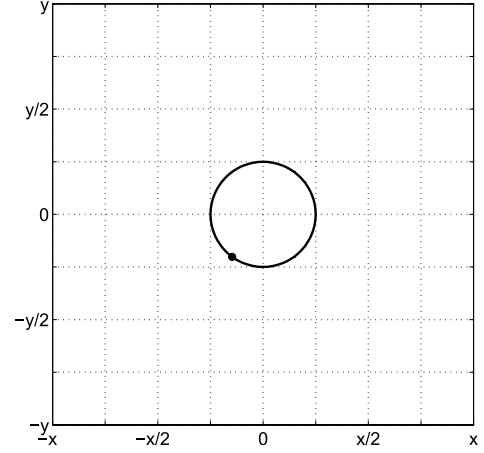


Fig. 3. Circular motion of a material point (denoted by the dot) with respect to the boundary. The coordinates change with the motion.

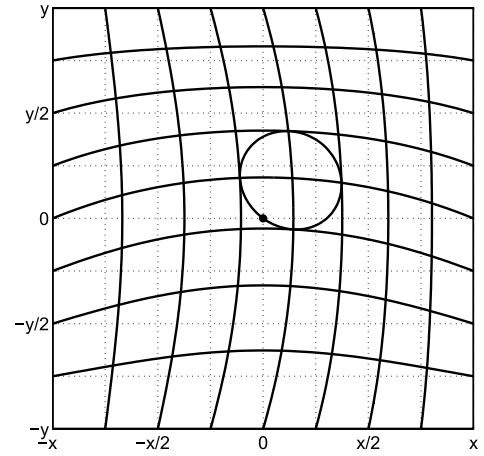


Fig. 4. Same circular motion, as in Fig. 3. Here, the coordinate of the material point is stationary and the metric tensor in \mathbb{R}^2 changes. The grid shown with solid lines and the circle represents the same points as the grid and circle of Fig. 3, respectively.

circular motion of a material point can be represented either by coordinates that change with the motion, Fig. 3, or by introducing motion into the metric tensor, see Fig. 4. Evidently, if we are able to describe the motion of a single point with the metric tensor, the same should apply to a set of material points as well. This is all that needs to be recognized to model the rotation of electrical machines with fixed coordinates.

IV. PULLBACK TO COORDINATE SYSTEMS

Since this paper focuses on rotating electrical machines, let us next examine in more depth the magnetic field in the so-called air gap. Let b and h be the magnetic flux and magnetomotive force, respectively. In addition, μ_E is permeability, \star_E is the Hodge operator, σ_E the unit 3-covector, and $\langle \cdot, \cdot \rangle$ the inner product implied by g_E .

At each point of space

$$\mu_E \langle h, h' \rangle_{\sigma_E} = \mu_E (\star_E h \wedge h') = b \wedge h' \quad (1)$$

should hold for all h' .

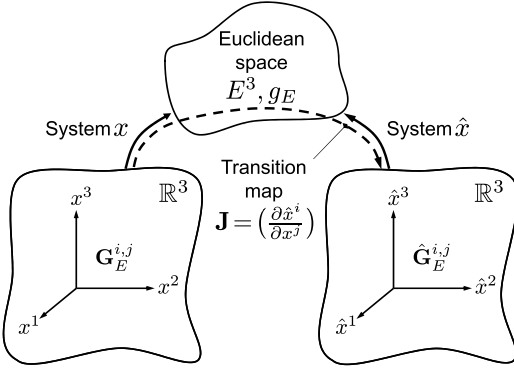


Fig. 5. Two coordinate systems x and \hat{x} label Euclidean space E^3 with coordinates. The transition map from x to \hat{x} provides us with a Jacobian matrix \mathbf{J} . In addition, the pullback of the metric tensor g_E to these systems x and \hat{x} yields matrices $\mathbf{G}_E^{i,j}$ and $\hat{\mathbf{G}}_E^{i,j}$, which are the counterparts of g_E in \mathbb{R}^3 , respectively.

Next, let us assume the points of E^3 are labeled by two coordinate systems x and \hat{x} , see Fig. 5. Every coordinate system labels the points of E^3 with some coordinates, and each system implies a canonical metric tensor—the identity matrix—into \mathbb{R}^3 . However, whatever coordinate system is employed, we want the metric tensor of \mathbb{R}^3 to match with that of E^3 , as this is where the model of physics “lives in.”

The so-called pullback of the metric tensor g_E to coordinate systems x and \hat{x} yield

$$(\mu_E \hat{\mathbf{G}}_E^{i,j} \hat{h}_i \hat{h}_j) \sigma_E = (\mu_E G_E^{i,j} h_i h_j) \sigma_E = \mu_E \langle h, h' \rangle \sigma_E \quad (2)$$

where

$$h_i dx^i = \hat{h}_i d\hat{x}^i = h \quad (3)$$

and $G_E^{i,j}$ and $\hat{G}_E^{i,j}$ are the representations of g_E in the x and \hat{x} systems, respectively.

With the aid of the transition map from x to \hat{x} system we may write

$$d\hat{x}^i = \frac{\partial \hat{x}^i}{\partial x^j} dx^j \quad (4)$$

and

$$\sigma dx = \sigma dx^1 \wedge dx^2 \wedge dx^3 = \sigma_E \quad (5)$$

$$\hat{\sigma} d\hat{x} = \hat{\sigma} d\hat{x}^1 \wedge d\hat{x}^2 \wedge d\hat{x}^3 = \sigma_E \quad (6)$$

where σ and $\hat{\sigma}$ are the real numbers. Their ratio is

$$\sigma / \hat{\sigma} = \det \mathbf{J} \quad (7)$$

where $\mathbf{J} = (\partial \hat{x}^i / \partial x^j)$ is the Jacobian matrix of the transition map.

Accordingly, we have now

$$\begin{aligned} (\mu_E \hat{\mathbf{G}}_E^{i,j} \hat{h}_i \hat{h}_j) \hat{\sigma} d\hat{x} &= \left(\mu_E \left(\frac{\partial \hat{x}^k}{\partial x^i} \right) G_E^{i,j} \left(\frac{\partial \hat{x}^l}{\partial x^j} \right) \hat{h}_k \hat{h}_l \right) \\ \sigma dx &= \left(\mu_E G_E^{i,j} \left(\frac{\partial \hat{x}^k}{\partial x^i} \hat{h}_k \right) \left(\frac{\partial \hat{x}^l}{\partial x^j} \hat{h}_l \right) \right) \\ \sigma dx &= (\mu_E G_E^{i,j} h_i h_j) \sigma dx = \mu_E \langle h, h' \rangle \sigma_E \end{aligned} \quad (8)$$

for all h' . Furthermore, we may write

$$\begin{aligned} (\mu_{\hat{x}}^{k,l} \hat{h}_k \hat{h}_l) d\hat{x} &= \left(\left(\frac{\partial \hat{x}^k}{\partial x^i} \right) \frac{\sigma \mu_E}{\det \mathbf{J}} G_E^{i,j} \left(\frac{\partial \hat{x}^l}{\partial x^j} \right) \hat{h}_k \hat{h}_l \right) \\ d\hat{x} &= (\mu_E \hat{\mathbf{G}}_E^{i,j} \hat{h}_i \hat{h}_j) \hat{\sigma} d\hat{x} \end{aligned} \quad (9)$$

for all h' , where

$$\mu_{\hat{x}}^{k,l} = \left(\frac{\partial \hat{x}^k}{\partial x^i} \right) \frac{\sigma \mu_E}{\det \mathbf{J}} G_E^{i,j} \left(\frac{\partial \hat{x}^l}{\partial x^j} \right) \quad (10)$$

is permeability in the \hat{x} system.

Summing up, if we know $G_E^{i,j}$, μ_E , and σ in the x -system, and the transition map from x to \hat{x} , then the bh-product $\mu_E \langle h, h' \rangle \sigma_E$ is expressed in the \hat{x} -system with (9).

V. IMPLEMENTATION INTO FINITE ELEMENTS

When solving the boundary value problems modeling electric machines with finite elements, the entries of the stiffness matrix are of the form

$$\int_{\Omega} \mu_E \langle h, h' \rangle \sigma_E \quad \text{or} \quad \int_{\Omega} \frac{1}{\mu_E} \langle b, b' \rangle \sigma_E$$

depending on whether a so-called h - or b -formulation is employed.

Typically, with finite elements one employs second-order boundary value problems by expressing the fields in terms of potentials. Therefore let dw and ζ_E stand for either h and μ_E or b and $1/\mu_E$, respectively. The entries of the finite element system matrix in terms of the x and \hat{x} system are

$$\begin{aligned} \int_{\Omega} (\zeta_{\hat{x}}^{k,l} d\hat{w}_k d\hat{w}_l) d\hat{x} &= \int_{\Omega} (\zeta_E G_E^{i,j} dw_i dw_j) \sigma dx \\ &= \int_{\Omega} \zeta_E \langle dw, dw' \rangle \sigma_E. \end{aligned} \quad (11)$$

Summing up, if we make the modeling decision to keep the coordinates of both the rotor and the stator stationary and call this system by name \hat{x} , then the rotation can be incorporated into matrix $\zeta_{\hat{x}}^{k,l}$ such that $\zeta_{\hat{x}}^{k,l}$ changes in time.

Remark 1: Only the metric dependent data needs to be updated in (11) at each time step. The exterior derivatives and σ_E are invariant to the changes in metric.

Remark 2: Let us translate (11) and (10) into the standard finite element language. In terms of vector analysis and Cartesian coordinates ($\mathbf{G}_E = \text{Id}$, $\sigma = 1$), we obtain in the air gap ($\mu_E = \mu_0$) for the h -formulation

$$\int_{\text{air gap}} (\mu_{\hat{x}} \text{grad } \psi) \cdot \text{grad } \psi' d\Omega_{\hat{x}}, \quad \mu_{\hat{x}} = \mu_0 \frac{\mathbf{J}\mathbf{J}^T}{\det \mathbf{J}} \quad (12)$$

and for the b -formulation

$$\int_{\text{air gap}} (\mathbf{v}_{\hat{x}} \text{curl } \mathbf{A}) \cdot \text{curl } \mathbf{A}' d\Omega_{\hat{x}}, \quad \mathbf{v}_{\hat{x}} = \frac{1}{\mu_0} \det(\mathbf{J}) \mathbf{J}^{-T} \mathbf{J}^{-1}. \quad (13)$$

Herein, ψ denotes the magnetic scalar potential, \mathbf{A} the magnetic vector potential, and $d\Omega_{\hat{x}}$ is the volume element of system \hat{x} . Notice also that the evaluation of the dot product and

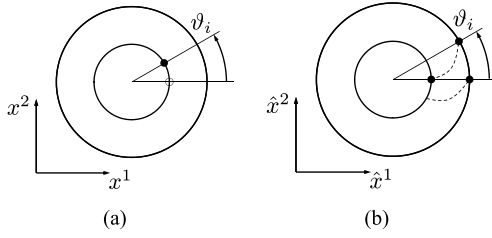


Fig. 6. Different ways of modeling rotation. (a) Rotation is considered in the x -system. The rotor has rotated by an angle ϑ_i from where it was at $t = t_0$. (b) Rotation is considered in the \hat{x} -system. Points, which are the closest to each other on the opposite sides of the air gap, need to be specified.

operators grad and curl retain here their usual Cartesian form. The impact of the nonstandard metric tensor $\hat{\mathbf{G}}_E$ is confined to the matrices $\boldsymbol{\mu}_{\hat{x}}$ and $\mathbf{v}_{\hat{x}}$, respectively.

Remark 3: If the fields have been computed with fixed mesh in the \hat{x} system, the results have to be interpreted with respect to this same system—not with respect to the x -system. When it comes to post-processing this implies that the nonstandard representation $\hat{\mathbf{G}}_E$ of the metric tensor has to be considered properly. More details on this are given in Appendix.

VI. CONSTRUCTION OF THE TRANSITION MAP

The remaining question is the choice of the transition map. This map can be specified in many ways. Here, we will introduce an approach that can be applied to various types of problems.

For this, let us first consider rotation in the x -system. Let us say that at moment $t = t_i$ the rotor has rotated by an angle $\vartheta = \vartheta_i$ from where it was at $t = t_0$, see Fig. 6(a). To express the same rotation in the \hat{x} system—in which the coordinates of the rotor and stator do not change from t_0 to t_1 —we need to specify pairwise the points, which are the closest to each other on the opposite sides of the air gap, see Fig. 6(b).

Since we know the coordinates of the opposite points in the x -system, we may take these as Dirichlet type of boundary conditions and solve for the x -coordinates inside the air gap with the Laplace equation. This then provides us with a desired transition map.

Remark 4: This is an example of what is called a boundary fitted coordinate system in the literature. The Laplace equation is called generating equation in this context [14].

From the numerical point of view, we prefer a transition map whose Jacobian determinant is everywhere one. For this reason, we solve the Laplace equation for the azimuthal coordinate ϕ only, and leave the other coordinates unchanged. In this case, $\det \mathbf{J} = 1$ amounts to $\partial\phi/\partial\hat{\phi} = 1$.

In electrical machines, the air gap is typically bounded by coaxial cylinders, with radii R_r and R_s , $R_r < R_s$. In such case, the Laplace equation can be solved analytically. The analytical solution, independent of $\hat{z} = \hat{x}^3$, is

$$\phi = g(\hat{r})\hat{\phi} + (1 - g(\hat{r}))(\hat{\phi} + \vartheta) \quad (14)$$

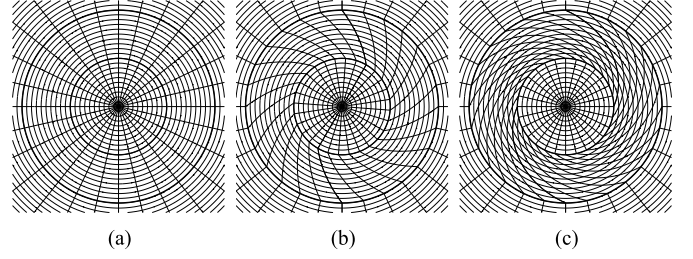


Fig. 7. Transition map $\hat{x} \mapsto x$ generated by solution of a Laplace problem for the cylindrical coordinate ϕ , while $r = \hat{r}$, $z = \hat{z}$. Coordinate lines in the air gap are given by (14).

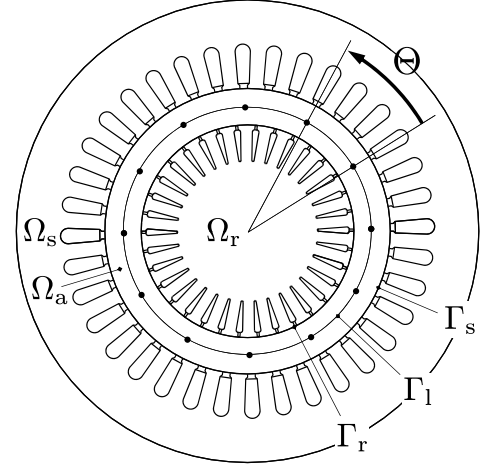


Fig. 8. Cross section of a typical electrical machine, the air gap is exaggerated. Rotor domain Ω_r , stator domain Ω_s , air-gap domain Ω_a . We assume that the air gap domain is split into two subdomains by a circular cylinder Γ_l (lock step), coaxial to the rotation axis of the machine. The finite element mesh on the cylinder shall be invariant with respect to rotation by lock-step angle Θ .

where the expression for $g(\hat{r})$ is

$$g(\hat{r}) = \frac{\ln \frac{\hat{r}}{R_r}}{\ln \frac{R_s}{R_r}}.$$

The resulting transition map is shown in Fig. 7. In this case $\det \mathbf{J} = 1$ holds everywhere for all ϑ .

VII. EXPLOITATION AND NUMERICS

Let us now examine in more detail tangible engineering examples. We aim at testing our ideas against the so-called lock-step or sliding surface method [15], [16]. Consider an electrical machine cross section and the corresponding finite element mesh according to Fig. 8. With the standard lock-step method, rotation of the rotor is divided into discrete steps of size Θ . However, since the finite element mesh is constructed in the \hat{x} system, rotation does not imply that the mesh needs to be changed at every time step. Accordingly, the lock-step method is easily relaxed to allow any time steps, and this enables one to employ adaptive time-integration techniques.

The theory itself admits mechanical rotation angles up to $\pm\pi$, but for numerical reasons, standard finite elements limit

this in practice. This motivates a combined approach, which we will call by name chart-metric method. Section VII-A explains how adjustable steps can be introduced in the lock-step method. Section VII-B elaborates on large rotations and the related numerical issues. A criterion for the choice of Θ will be discussed and presented in Section VIII-B. A description of how the presented approach could be implemented in a finite element software system is given in Appendix.

A. Introduction of Adjustable Steps into Lock-Step Method

The standard lock-step method requires a situation similar to Fig. 8. The finite element mesh shall be prepared in such a way that the circular cylinder Γ_l (approximately) consists of a union of element interfaces. Moreover, the mesh on the cylinder shall be invariant with respect to rotation around the machine axis by lock-step angle Θ . In other words, mesh reconnection at Γ_l with angular displacements that are integer multiples of Θ is supported. This setting serves as our starting point.

With the chart-metric method, small angular displacements $|\vartheta| < \Theta$ are treated by changing the metric of the coordinate system, while angular displacements greater than Θ trigger a mesh reconnection at Γ_l .

Consider a small rotation angle $|\vartheta| < \Theta$. In this case, we solve for the electromagnetic problem in the \hat{x} -system, with fixed mesh. Now assume the rotation angle is growing, such that eventually $\vartheta = \Theta$ holds. We are able to map all objects of interest (mesh, data, etc.) bijectively from the \hat{x} system to the x -system, using the transition map $x \mapsto \hat{x}$.

Next, we eliminate the mesh distortion caused by the rotation. We reconnect the mesh at Γ_l with angular displacement of Θ . This constitutes a new mesh. By construction, the previous and the new mesh coincide in domains Ω_r and Ω_s , respectively. Since the subdomain Ω_a is nonconducting, initial values within a time stepping scheme are not required. The prolongation of data from the previous to the new mesh in this subdomain can just be ignored. Therefore, there is no need to remap any data.

After this procedure has been accomplished, the previous x -system takes the role of new \hat{x} system, and the rotation angle ϑ starts from zero again.

Remark 5: An improvement can be achieved by limiting small angular displacements to $|\vartheta| < \Theta/2$, and performing reconnection once this range has been left.

Remark 6: In a fluid dynamics context, the presented approach falls in the category of arbitrary Lagrangian–Eulerian methods [17], [18].

B. Large Rotations and Related Numerical Issues

At this point, a rather obvious question emerges, what happens numerically when the rotation angle becomes large? Modeling large rotation angles with the metric tensor of system \hat{x} corresponds to rather severely deformed elements in the standard x -system, see Fig. 7(c). Before working the details out, let us emphasize that the underlying theoretical framework relies on Riemannian geometry.

However, as soon as finite-dimensional approximations are employed, numerical issues may appear. For, the limited approximation capability of low-order finite element basis functions implies the solutions may converge only slowly toward the right ones upon refinement of the finite element meshes.

The condition number $\text{cond} \mu_{\hat{x}}$ of the permeability matrix defined in (12) indicates the deformation. We start from the transition map in terms of the azimuthal coordinate, as presented in Section VI, and let $(\hat{x}, \hat{y}, \hat{z}) = (\hat{x}^1, \hat{x}^2, \hat{x}^3)$, $u = \phi - \hat{\phi}$ hold. The inverse transition map is then

$$\begin{pmatrix} x \\ y \\ z \end{pmatrix} = \mathbf{R} \begin{pmatrix} \hat{x} \\ \hat{y} \\ \hat{z} \end{pmatrix}, \quad \mathbf{R} = \mathbf{R}(u(\hat{x}, \hat{y}, \hat{z})) \quad (15)$$

with the rotation matrix

$$\mathbf{R} = \mathbf{R}(u) = \begin{pmatrix} \cos u & -\sin u & 0 \\ \sin u & \cos u & 0 \\ 0 & 0 & 1 \end{pmatrix}. \quad (16)$$

The Jacobian matrix of the transition map can be obtained by differentiating (15)

$$\mathbf{J} = (\mathbf{R} + \mathbf{R}'\mathbf{S})^{-1}$$

where

$$\mathbf{R}'(u) = \begin{pmatrix} -\sin u & -\cos u & 0 \\ \cos u & -\sin u & 0 \\ 0 & 0 & 0 \end{pmatrix}$$

$$\mathbf{S} = \begin{pmatrix} \hat{x} \\ \hat{y} \\ 0 \end{pmatrix} \begin{pmatrix} \frac{\partial u}{\partial \hat{x}} & \frac{\partial u}{\partial \hat{y}} & \frac{\partial u}{\partial \hat{z}} \end{pmatrix}.$$

Remark 7: The transition map features translational symmetry with respect to \hat{z} provided that $\partial u / \partial \hat{z} = 0$ holds. In this case, the Jacobian matrix has the form

$$\mathbf{J} = \begin{pmatrix} \mathbf{J}_2 & 0 \\ 0 & 1 \end{pmatrix}.$$

We consider the analytical solution (14), as a special case. In addition to the translational symmetry the function u exhibits rotational symmetry, that is, $\partial u / \partial \hat{\phi} = 0$ holds. Then

$$\begin{pmatrix} \hat{x} \\ \hat{y} \\ 0 \end{pmatrix} = \hat{r} \mathbf{e}(\hat{\phi}), \quad \mathbf{e}(\hat{\phi}) = \begin{pmatrix} \cos \hat{\phi} \\ \sin \hat{\phi} \\ 0 \end{pmatrix}, \quad \left(\frac{\partial u}{\partial \hat{x}} \frac{\partial u}{\partial \hat{y}} \frac{\partial u}{\partial \hat{z}} \right)^T = \mathbf{e}(\hat{\phi}) \frac{\partial u}{\partial \hat{r}}$$

so that \mathbf{S} in (17) reads

$$\mathbf{S} = c \mathbf{e}(\hat{\phi}) \mathbf{e}^T(\hat{\phi}), \quad c = \hat{r} \frac{\partial u}{\partial \hat{r}} = -\frac{\vartheta}{\ln \frac{R_s}{R_r}}$$

where we used $u = \vartheta(1 - g(\hat{r}))$ from (14). Moreover, we find from (17)

$$\mathbf{J}^{-1} = \mathbf{R}(u) \left(\mathbf{I} + \mathbf{R} \left(\frac{\pi}{2} \right) \mathbf{S} \right)$$

where we considered $\mathbf{R}'(u)\mathbf{S} = \mathbf{R}(u + \pi/2)\mathbf{S}$, and the Abelian group property $\mathbf{R}(u)\mathbf{R}(v) = \mathbf{R}(v)\mathbf{R}(u) = \mathbf{R}(u + v)$. Next, we compute

$$\mathbf{R}(-\hat{\phi})\mathbf{J}^{-1}\mathbf{R}(\hat{\phi}) = \mathbf{R}(u) \begin{pmatrix} 1 & 0 & 0 \\ c & 1 & 0 \\ 0 & 0 & 1 \end{pmatrix}$$

so that

$$\mathbf{R}(-\hat{\phi})\mathbf{J}^{-T}\mathbf{J}^{-1}\mathbf{R}(\hat{\phi}) = \begin{pmatrix} 1 + c^2 & c & 0 \\ c & 1 & 0 \\ 0 & 0 & 1 \end{pmatrix}.$$

From this we obtain with (12) the intermediate result

$$\text{cond } \mu_{\hat{x}} = \text{cond} \begin{pmatrix} 1 + c^2 & c & 0 \\ c & 1 & 0 \\ 0 & 0 & 1 \end{pmatrix}$$

since the condition number is invariant under orthogonal transformations $\mathbf{R}(\hat{\phi})$. The eigenvalues are

$$\lambda_{1,2} = 1 + \frac{c^2}{2} \pm c\sqrt{1 + \frac{c^2}{4}} > 0, \quad \lambda_1\lambda_2 = 1, \quad \lambda_3 = 1$$

hence

$$\text{cond } \mu_{\hat{x}} = \left(\frac{|c|}{2} + \sqrt{1 + \left(\frac{|c|}{2}\right)^2} \right)^4, \quad |c| = \frac{\vartheta}{\ln \frac{R_s}{R_r}}. \quad (17)$$

Let us denote the air-gap width by $\delta = R_s - R_r$. For typical electrical machines, $\delta/R_r \ll 1$. For instance, for the test case presented in Section VIII ratio $\delta/R_r \approx 6 \cdot 10^{-3}$. In this case, we may approximate $|c|$ by $\vartheta R_r/\delta$. The maximum condition number is obtained for $\vartheta = \Theta/2$. Note that for increasing ϑ , we have

$$\text{cond } \mu_{\hat{x}} = \mathcal{O} \left(\frac{\vartheta R_r}{\delta} \right)^4. \quad (18)$$

VIII. TEST EXAMPLE

A. Definition of Test Example

In this section, the start-up of an induction motor under no-load conditions is examined. A three-phase cage induction motor is considered, whose cross section can be observed in Fig. 9. Some parameters of the test motor are collected in Table I. The test case is a slightly simplified version of the 15 kW motor presented in [19, Sec. 3.3.4] and in [20], respectively. Note that, we aim at discussing the metric-based treatment of motion rather than producing results to be compared against the data in the references.

The following modeling assumptions regarding the details of the machine have been made. The magnetic field in the motor is assumed to be 2-D, end effects are neglected, as well as the skew of the slots. The current density in the stator conductors is regarded to be constant. The iron core is treated as a nonconducting magnetically nonlinear medium without any hysteresis. Hence, the magnetic properties of the iron core are described by a magnetization curve, with initial relative permeability of 1.600 and saturation induction of 2 T.

The electromagnetic field in the motor is described by a standard 2-D $\mathbf{A}-\varphi$ formulation with a single component vector

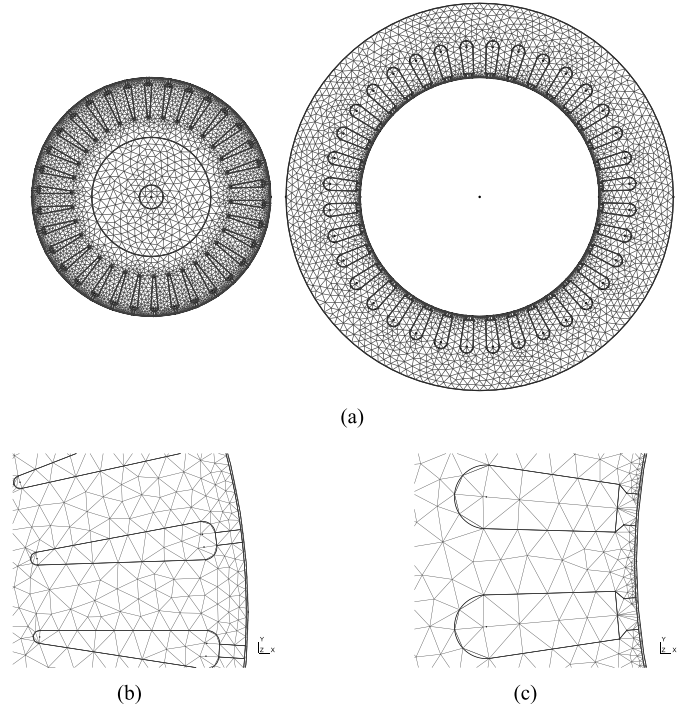


Fig. 9. Finite element mesh in the cross section of the induction motor. (a) Rotor and stator. (b) Rotor (zoomed-in-view). (c) Stator (zoomed-in-view).

TABLE I
SOME PARAMETERS OF THE TEST MOTOR

Number of pole pairs	$p = 2$
Number of stator / rotor slots	36 / 34
Stator outer radius	117.5 mm
Rotor outer radius	$R_r = 72.5$ mm
Air-gap width	$\delta = 0.45$ mm
Core length	$L = 195$ mm
Resistance of each stator winding	0.1 Ω
Number of conductors per slot	15
Connection	star
Phase voltage rms	$U = 230$ V
Frequency	$f = 50$ Hz
Conductivity of rotor bars	$57 \cdot 10^6$ S/m (Cu)

potential \mathbf{A} , and a electric scalar potential φ whose support is the union of all rotor bars, and which exhibits constant gradient in each bar [20, eqs. (1), (4)]. A homogeneous Dirichlet condition is set for \mathbf{A} on the outer boundary of the stator.

The star-connected stator windings a, b, and c are driven by a symmetric voltage

$$\left. \begin{aligned} u_a(t) &= -\sqrt{2}U \cos(2\pi ft), \\ u_b(t) &= -\sqrt{2}U \cos(2\pi ft + 2\pi/3), \\ u_c(t) &= -\sqrt{2}U \cos(2\pi ft + 4\pi/3) \end{aligned} \right\}. \quad (19)$$

Voltage drive requires an additional equation for each stator winding [21, eq. (4)]. Eventually, Kirchhoff current law has to be enforced explicitly for the rotor bars, by another additional equation. That is, the sum of all rotor bar currents must be zero. Since the number of rotor bars (=34) is not divisible by the number of poles (=4) this condition is not automatically satisfied by symmetry.

The finite element mesh was generated by the public domain software GMSH [22], and has 8.843 nodes and

16.624 triangular elements. Linear basis functions are associated to the nodes and quadratic basis functions to the edges of the mesh, resulting in about 33.000 degrees of freedom.

The simulations have been performed with the public domain software GETDP [23]. Each simulation is started at $t_0 = 0$, with $\mathbf{A} = 0$ as initial condition, and rotor at rest. At this point, the stator windings are connected to the symmetric voltage (19). The backward Euler scheme is applied for time stepping. Following [19, Sec. 3.4], a fixed time step of $\Delta t = 100 \mu\text{s}$ was chosen. Numerical experiments with different time steps confirmed that this choice offers a good compromise between the efficiency and the accuracy. 2.000 time steps covered a time interval of 200 ms, after which the transient phenomena had practically disappeared.

At each time step, the field and circuit equations are solved, which yields updated values of the vector potential. This is accomplished by Newton-Raphson method relying on a direct solver. Hence, nonlinear and dynamic effects are included in the model without principle restrictions. Next, the torque on the rotor is computed in the same manner as Arkkio did [20, eq. (9)], see Appendix. Finally, the equation of motion is solved for the rotor, to determine its new position for the next time step. To this end, the rotor was assigned a moment of inertia of $0.066 \text{ kg}\cdot\text{m}^2$, which corresponds to a steel cylinder of the same size.

In contrast to [20], where the mesh in the air gap changed at each time step, we applied the algorithm described in Section VII-A, in connection with the analytical expression (14) for the inverse transition map $(\hat{r}, \hat{\phi}) \mapsto (r, \phi)$. The circle Γ_l was subdivided uniformly by $N = 456$ nodes, which yields a lock-step angle of $\Theta = 2\pi/N \approx 1.4 \cdot 10^{-2} \text{ rad} \approx 0.79^\circ$. With this choice, we receive from (17)

$$\max \text{cond } \mu_{\hat{x}} \approx 8.4$$

which was deemed feasible. How the choice of Θ affects the numerical results will be discussed in the next section. Moreover, at synchronous speed the motor rotates during one time step by

$$\frac{2\pi f}{p} \cdot \Delta t \approx 1.6 \cdot 10^{-2} \text{ rad} \approx 0.9^\circ$$

which indicates a good balance of temporal and spatial discretization.

B. Results and Discussion

1) *Results:* Fig. 10 shows the simulation results for the start-up of the induction motor under no-load conditions. After a transient period, the synchronous speed of 25 r/s is attained. A commercial code (vector fields Opera-2d) was used for validating results. When given identical trajectories, our approach produces good agreement (typically within a few percents) with the commercial code. Identical trajectories were needed since small differences in the torques tend to accumulate as differences in angular velocities.

Since the formulation outside the air gap is equivalent to standard time-domain FE methods, the solution time is mostly

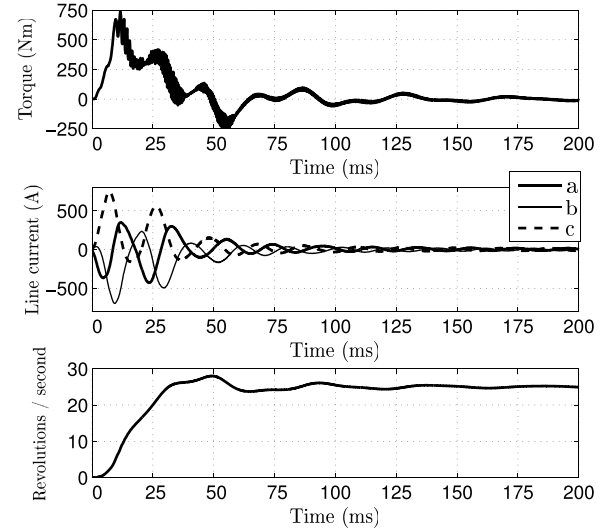


Fig. 10. Start-up of the induction motor under no-load conditions, star-connected, 230 V r/s 50 Hz source voltage, $\Delta t = 100 \mu\text{s}$ time stepping. Rotation by chart-metric method. The topmost and middle figures show the electromagnetic torque acting on the rotor and the line currents of the three-phase system, respectively.

determined by the discretization used. The average solution time per time step on 1.8 GHz Intel i5-3427U was about 13.4 s for the chart-metric method and 10.1 s for the lock-step method. This suggests that the cost-benefit ratio of the chart-metric method is well acceptable.

The effectiveness of the algorithm is evident from Fig. 11, which exhibits an intricate combination of numerical efficiency and precision. Time steps, which lead to small angular displacements, are treated by changes in metric. Each solid line corresponds to a sequence of such time steps. If the modulus of the reduced rotation angle ψ according to (21) exceeds $\Theta/2$, a lock step is executed, to reduce the large displacement to a small one. The spatial and temporal discretizations of the boundary value problem become decoupled. For the scheme with fixed time steps, the benefit is greatest in the start. Even bigger advantage would be derived for an adaptive time stepping scheme, where the step sizes are not known in advance.

2) *Large Rotations:* We pointed out in Section VII-B that modeling large rotation angles with the metric tensor corresponds to rather severely deformed elements in the standard system. This effect can be quantified by considering the condition number $\text{cond } \mu_{\hat{x}}$ of the permeability matrix. Informally, the heuristic explanation is, the larger the rotation angle, the more anisotropic the air gap appears, to guide the flux along the circumferential direction. Equation (18) reveals that the condition number grows asymptotically with the fourth power of the rotation angle. This effect can be observed from Fig. 12. If the admissible range for the reduced rotation angle increases by a factor of four, the maximum condition number rises from 8.4 to 470. This situation typically occurs before a lock step is executed. The deviation of the dashed from the thick solid line in Fig. 12 shows a deterioration of accuracy due to this effect. Therefore, as a rule, the lock-step angle Θ should be

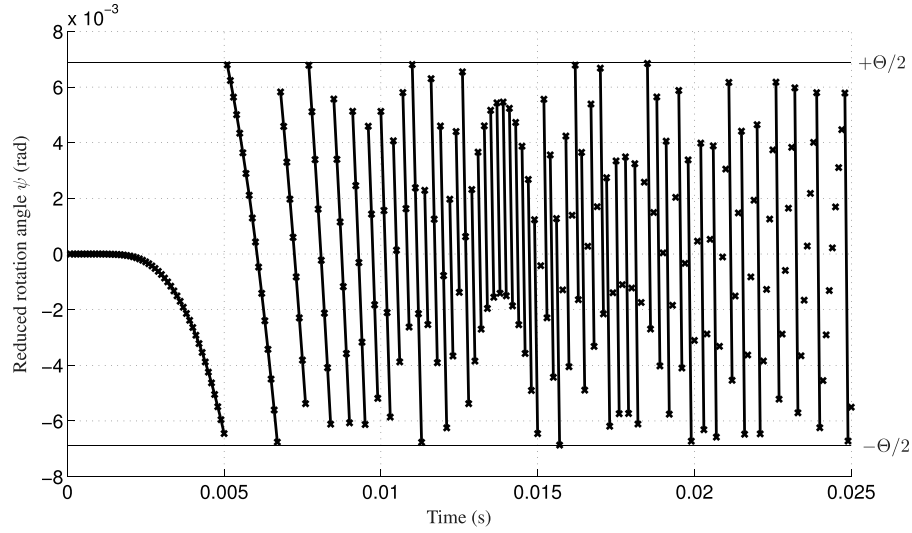


Fig. 11. Chart-metric method in the simulation according to Fig. 10. Each solid line corresponds to a sequence of time steps without a lock step.

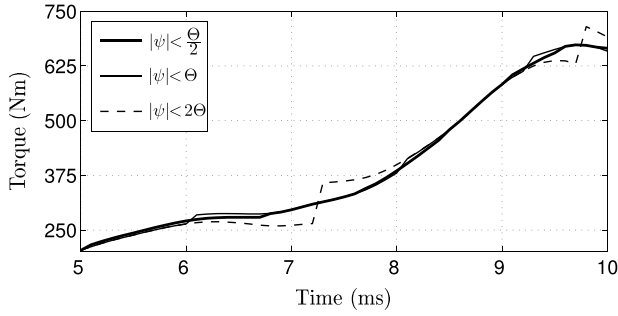


Fig. 12. Comparison of the torque evolution over some time interval for larger metric-based rotations. The original range $|\psi| < \Theta/2$ for the reduced rotation angle is compared with ranges two and four times as big. Accuracy is deteriorated if the admissible range is chosen too big.

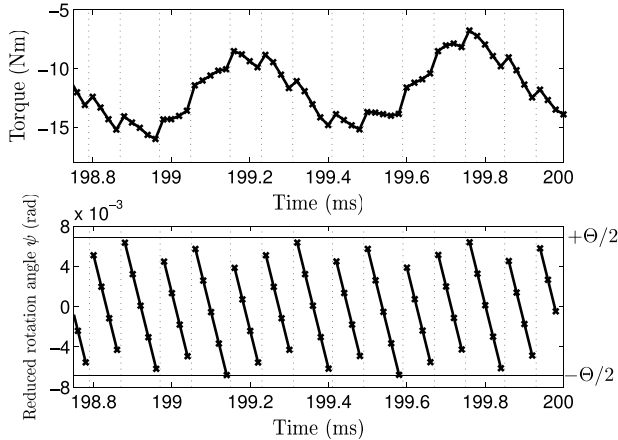


Fig. 13. Torque and reduced rotation angle near steady state, compare with Figs. 10 and 11. The time step was reduced to $\Delta t/5 = 20 \mu s$, to better display the remaining small ripple. Dotted vertical lines correspond to lock steps.

chosen according to

$$\Theta \approx \frac{2\delta}{R_r}. \quad (20)$$

When the ratio of the lock-step angle to the rotation per time step is large, lock steps can be observed to cause a small ripple in the steady-state torque even if (20) is satisfied, see Fig. 13.

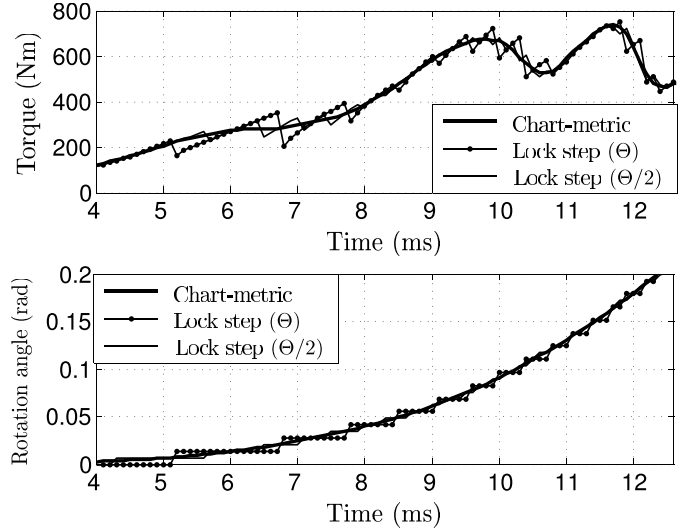


Fig. 14. Torques and rotation angles from simulations with 1) chart-metric method and 2) pure lock-step rotation. Two different lock-step sizes were considered in case 2), corresponding to two different mesh densities on the circle Γ_l .

3) *Comparison With Lock-Step Technique:* We compared the chart-metric method with a pure lock-step approach. To that end, the lock-step which best fitted the actual rotor position was picked in each time step, and the metric-based rotation was skipped. The additional discretization introduces undesired noise in the torque curve, compare Fig. 14. Since the lock-step angle Θ corresponds to one element edge on the circle Γ_l , the noise can be reduced by making the mesh denser. However, because the chart-metric method is performed in a mesh with only 456 nodes on the circle Γ_l , getting rid of the noise with pure lock-step rotation would require a much denser mesh. We conclude that coupling of space and time discretizations via the lock step impacts the simulation efficiency.

IX. CONCLUSION

Coordinate systems label points of manifolds. Therefore, one has all the freedom to select any chart and only thereafter work out how the metric tensor of the manifold becomes

represented in the chosen coordinate system. When it comes to modeling rotating electrical machines with finite elements, this implies that one may first select the coordinates of the rotor and stator and fix the finite element mesh to these coordinates. The rotation itself can be considered via specification of the distances between the points with a metric tensor as desired. The spatial and temporal discretizations become advantageously decoupled, i.e., any time step in the numerical solution of the boundary value problem can be employed. The test example demonstrates some practical advantages of such an approach when solving numerically boundary value problems modeling rotating machines.

APPENDIX

FINITE ELEMENT IMPLEMENTATION OF CHART-METRIC METHOD

We describe how the chart-metric method presented in Section VII-A could be implemented in a finite element software system. We present a high abstraction procedural description of the most important steps, with some existing time-stepping scheme in mind. Derivation of more specific (pseudo)code should be straightforward.

A. Preparation of Time-Stepping

Before execution of time-stepping, perform the following tasks.

- 1) Prepare a mesh according to Fig. 8. Assign $N = 2\pi/\Theta$ and $k = 0$. Index k is used to keep track of the mesh connection.
- 2) Prepare data structures to solve the boundary value problem $\Delta u = 0$ with Dirichlet conditions on the boundaries Γ_s , Γ_r . Note that the boundaries Γ_s , Γ_r need not to be circular cylinders. The remaining boundaries of the domain Ω_a receive homogeneous Neumann conditions.

B. Execution of Time-Stepping

Given the desired rotation angle ϑ , perform the following steps.

- 1) Determine index

$$j = \operatorname{argmin}_{j \in [0, N-1]} |(\vartheta - j\Theta) \bmod 2\pi|.$$

If $j = k$, jump to step 3).

- 2) Mesh reconnection: reconnect the meshes with rotor rotated by $j\Theta$, relative to discretized position. Let $k = j$.
- 3) Assign

$$\psi = \vartheta - k\Theta \quad (21)$$

the reduced rotation angle. Note that $|\psi| \leq \Theta/2$.

- 4) Coordinate generation: solve the boundary value problem

$$\left. \begin{aligned} \Delta u &= 0, & \text{in } \Omega_a \\ u &= 0, & \text{on } \Gamma_s \\ u &= \psi, & \text{on } \Gamma_r \end{aligned} \right\}$$

numerically; compare to Fig. 8. This yields the nodal values of u in $\bar{\Omega}_a$. Compute the gradients $(\partial u / \partial \hat{x}, \partial u / \partial \hat{y}, \partial u / \partial \hat{z})$.

The boundary value problem is obtained from the Laplace problem for ϕ according to Section VI by the ansatz $\phi = \hat{\phi} + u$.

- 5) Jacobian matrix computation: form the matrices \mathbf{R} , \mathbf{R}' , \mathbf{S} , \mathbf{J} at the integration points of the finite elements, according to (16) and (17), respectively.
- 6) Metric modification: depending on the formulation, replace the air-gap permeability μ_0 by the matrix $\boldsymbol{\mu}_{\hat{x}}$ according to (12), or reluctivity $1/\mu_0$ by matrix $\boldsymbol{\nu}_{\hat{x}}$ according to (13), respectively.
- 7) Solve for the electromagnetic problem in the entire problem domain. Complete time step, which might involve force and torque computation (see next section), solution of the mechanical equations, and more. Go to step 1).

C. Postprocessing

As far as postprocessing is concerned, any standard approach can be employed in the stator domain Ω_s . Only slight modification is required in the rotor domain Ω_r , since the system \hat{x} is rotated with respect to the system x . This has to be considered for the computation of vectorial quantities. In contrast, the air-gap domain Ω_a was modeled in the \hat{x} system with nonstandard metric representation $\hat{\mathbf{G}}_E$; this requires some care.

If Cartesian coordinates are used for the x -system ($\mathbf{G}_E = \mathbf{Id}$), there is no difference between the covariant and contravariant components of a vector in this system. The situation is different in the \hat{x} -system, where the components of the vector potential $\hat{\mathbf{A}}$ obtained from the implementation according to Section V are the covariant components. Therefore, the transformation of the potentials from the \hat{x} system back to the x -system reads

$$\left. \begin{aligned} \psi(x) &= \hat{\psi}(\hat{x}) && \text{scalar,} \\ \mathbf{A}(x) &= J^T \hat{\mathbf{A}}(\hat{x}) && \text{covariant vector} \end{aligned} \right\}. \quad (22)$$

From that point on further computations, for example fields from potentials, can be accomplished in the x -system as usual.

Integral quantities often contain integrals that extend over the air gap. In this case, it is helpful to start from the standard system x , where the relevant expressions are known from textbooks or even implemented in the software. Then, the terms are transformed to the \hat{x} -system, using the transition map and its Jacobian, because it is this system that hosts the finite element discretization. Eventually, relations (22) are substituted, to arrive at an expression, which can be entirely evaluated in terms of the finite elements and their degrees of freedom.

We will explain this approach for the torque computation by Arkkio's method [20, eq. (9)], that was employed in Section VIII. For the torque on the rotor, it holds in the standard system x

$$T = \frac{L}{\mu_0 \delta} \int_{\Omega_x} r B_r B_\phi \, d\Omega_x$$

where L and δ have been introduced in Table I, $\Omega_x \subset \mathbb{R}^2$ denotes the cross section of the air-gap domain in the x -system, and $d\Omega_x = dx^1 dx^2$ holds. The field components

refer to polar coordinates (r, ϕ) . The torque can be expressed in terms of the vector potential \mathbf{A} , whose single x^3 -directed component is $a = a(x)$

$$T = \int_{\Omega_x} \text{rf} \left(\frac{\partial a}{\partial r}, \frac{1}{r} \frac{\partial a}{\partial \phi} \right) d\Omega_x$$

where

$$f(u, v) = -\frac{L}{\mu_0 \sigma} uv, \quad u = \frac{\partial a}{\partial r}, \quad v = \frac{1}{r} \frac{\partial a}{\partial \phi}. \quad (23)$$

For the transition map according to (14) the Jacobian matrix can be expressed by \mathbf{J}_2 , compare Remark 7. Then, (22) implies $\hat{a}(\hat{x}) = a(x)$, and by the chain rule

$$\left(\frac{\partial a}{\partial r}, \frac{1}{r} \frac{\partial a}{\partial \phi} \right) = \left(\frac{\partial \hat{a}}{\partial \hat{x}}, \frac{\partial \hat{a}}{\partial \hat{y}} \right) \mathbf{J}_2 \mathbf{R}_2(\phi),$$

$$\mathbf{R}_2(\phi) = \begin{pmatrix} \cos \phi & -\sin \phi \\ \sin \phi & \cos \phi \end{pmatrix}.$$

According to the transformation rule for multiple integrals, the torque can now be rewritten as

$$T = \int_{\Omega_{\hat{x}}} \text{rf} \left(\left(\frac{\partial \hat{a}}{\partial \hat{x}}, \frac{\partial \hat{a}}{\partial \hat{y}} \right) \mathbf{J}_2 \mathbf{R}_2(\phi) \right) \frac{1}{\det \mathbf{J}_2} d\Omega_{\hat{x}}$$

where r, ϕ , and \mathbf{J}_2 have to be understood as functions of (\hat{x}, \hat{y}) , and $\Omega_{\hat{x}}$ denotes the cross section of the air-gap domain in the \hat{x} system, $d\Omega_{\hat{x}} = d\hat{x}d\hat{y}$.

ACKNOWLEDGMENT

This work was partially funded by Tekes, the Finnish Funding Agency for Technology and Innovation, FiDiPro project 1481/31/09, Advanced Electromagnetic Modeling and Simulation for Engineering.

REFERENCES

- [1] A. Abdel-Razek, J. Coulomb, M. Feliachi, and J. Sabonnadière, "Conception of an air-gap element for the dynamic analysis of the electromagnetic field in electric machines," *IEEE Trans. Magn.*, vol. 18, no. 2, pp. 655–659, Mar. 1982.
- [2] F. Bouillault and A. Razek, "Hybrid numerical methods for movement consideration in electromagnetic systems," *IEEE Trans. Magn.*, vol. 24, no. 1, pp. 259–261, Jan. 1988.
- [3] D. Rodger, H. Lai, and P. Leonard, "Coupled elements for problems involving movement," *IEEE Trans. Magn.*, vol. 26, no. 2, pp. 548–550, Mar. 1990.
- [4] E. Lange, F. Henrotte, and K. Hameyer, "Biorthogonal shape functions for nonconforming sliding interfaces in 3-D electrical machine FE models with motion," *IEEE Trans. Magn.*, vol. 48, no. 2, pp. 855–858, Feb. 2012.
- [5] F. Rapetti, A. Buffa, F. Bouillault, and Y. Maday, "Simulation of a coupled magneto-mechanical system through the sliding-mesh mortar element method," *Int. J. COMPEL*, vol. 19, no. 2, pp. 332–340, 2000.
- [6] S. Böhmer, E. Lange, M. Hafner, T. Cramer, C. Bischof, and K. Hameyer, "Mesh decomposition for efficient parallel computing of electrical machines by means of FEM accounting for motion," *IEEE Trans. Magn.*, vol. 48, no. 2, pp. 891–894, Feb. 2012.
- [7] E. Coppoli, R. Mesquita, and R. Silva, "Induction machines modeling with meshless methods," *IEEE Trans. Magn.*, vol. 48, no. 2, pp. 847–850, Feb. 2012.
- [8] G. Krebs, T. Henneron, S. Clénet, and Y. Le Bihan, "Overlapping finite elements used to connect non-conforming meshes in 3-D with a vector potential formulation," *IEEE Trans. Magn.*, vol. 47, no. 5, pp. 1218–1221, May 2011.
- [9] Z. Wang, T. Henneron, N. Nemitz, J.-C. Mipo, and F. Piriou, "Electromagnetic field projection on finite element overlapping domains," *IEEE Trans. Magn.*, vol. 49, no. 4, pp. 1290–1298, Apr. 2013.
- [10] X. Shi, Y. Le Menach, J.-P. Ducreux, and F. Piriou, "Comparison between the mortar element method and the polynomial interpolation method to model movement in the finite element method," *IEEE Trans. Magn.*, vol. 44, no. 6, pp. 1314–1317, Jun. 2008.
- [11] S. Niu, S. Ho, W. Fu, and J. Zhu, "A convenient mesh rotation method of finite element analysis using sub-matrix transformation approach," *IEEE Trans. Magn.*, vol. 48, no. 2, pp. 303–306, Feb. 2012.
- [12] L. Kettunen, S. Kurz, A. Stenvall, S. Suuriniemi, and T. Tarhasaari. (2013). *Motion and Metric* [Online]. Available: <http://youtu.be/UAKKwZg3fkW>
- [13] P. Raunonen, "Mathematical structures for dimensional reduction and equivalence classification of electromagnetic boundary value problems," Ph.D. dissertation, Tampere Univ. Technol., Tampere, Finland, 2009.
- [14] J. Thompson, Z. Warsi, and C. Mastin, "Boundary-fitted coordinate systems for numerical solution of partial differential equations—A review," *J. Comput. Phys.*, vol. 47, no. 1, pp. 1–108, 1982.
- [15] R. Perrin-Bit and J. Coulomb, "A three-dimensional finite element mesh connection for problems involving movement," *IEEE Trans. Magn.*, vol. 31, no. 3, pp. 1920–1923, May 1995.
- [16] T. Preston, A. Reece, and P. Sangha, "Induction motor analysis by time-stepping techniques," *IEEE Trans. Magn.*, vol. 24, no. 1, pp. 471–474, Jan. 1988.
- [17] J. Donea, A. Huerta, J.-P. Ponthot, and A. Rodríguez-Ferran, "Arbitrary Lagrangian-Eulerian methods," in *Encyclopedia of Computational Mechanics*. New York, NY, USA: Wiley, 2004.
- [18] R. Rieben, D. White, B. Wallin, and J. Solberg, "An arbitrary Lagrangian-Eulerian discretization of MHD on 3D unstructured grids," *J. Comput. Phys.*, vol. 226, no. 1, pp. 534–570, 2007.
- [19] A. Arkkio, "Analysis of induction motors based on the numerical solution of the magnetic field and circuit equations," Ph.D. dissertation, Acta Polytechnica Scandinavia, Helsinki Univ. Technol., Helsinki, Finland, Dec. 1987.
- [20] A. Arkkio, "Finite element analysis of cage induction motors fed by static frequency converters," *IEEE Trans. Magn.*, vol. 26, no. 2, pp. 551–554, Mar. 1990.
- [21] P. Leonard and D. Rodger, "Voltage forced coils for 3D finite-element electromagnetic models," *IEEE Trans. Magn.*, vol. 24, no. 6, pp. 2579–2581, Nov. 1988.
- [22] C. Geuzaine and J. Remacle, "Gmsh: A three-dimensional finite element mesh generator with built-in pre- and post-processing facilities," *Int. J. Numer. Methods Eng.*, vol. 79, no. 11, pp. 1309–1331, 2009.
- [23] P. Dular, C. Geuzaine, F. Henrotte, and W. Legros, "A general environment for the treatment of discrete problems and its application to the finite element method," *IEEE Trans. Magn.*, vol. 34, no. 5, pp. 3395–3398, Sep. 1998.